Nanoscale

Enhanced lithium storage in Fe$_2$O$_3$–SnO$_2$–C nanocomposite anode with a breathable structure†

Md Mokhlesur Rahman,* Alexey M. Glushenkov, Thrinathreddy Ramireddy, Tao Tao and Ying Chen*

A novel nanocomposite architecture of a Fe$_2$O$_3$–SnO$_2$–C anode, based on clusters of Fe$_2$O$_3$ and SnO$_2$ nanoparticles dispersed along the conductive chains of Super P Li™ carbon black (Timcal Ltd.), is presented as a breathable structure in this paper for lithium-ion batteries. The synthesis of the nanocomposite is achieved by combining a molten salt precipitation process and a ball milling method for the first time. The crystalline structure, morphology, and electrochemical characterization of the synthesised product are investigated systematically. Electrochemical results demonstrate that the reversible capacity of the composite anode is 1110 mA h g^{-1} at a current rate of 158 mA g^{-1} with only 31% of initial irreversible capacity in the first cycle. A high reversible capacity of 502 mA h g^{-1} (higher than the theoretical capacity of graphite, $\sim$372 mA h g^{-1}) can be obtained at a high current rate of 3950 mA g^{-1}. The electrochemical performance is compared favourably with those of Fe$_2$O$_3$–SnO$_2$ and Fe$_2$O$_3$–SnO$_2$–C composite anodes for lithium-ion batteries reported in the literature. This work reports a promising method for the design and preparation of nanocomposite electrodes for lithium-ion batteries.

Introduction

Lithium-ion batteries are a promising practical technology for more efficient electrochemical storage of energy.[1,2] In the past decade, nanostructured electrode materials have been extensively studied due to their potential to deliver higher energy and power densities and longer cycle life in next-generation lithium-ion batteries.[3–5] The anode is one of the major components of the battery, and graphite is currently used as the main commercial anode material in the lithium-ion technology. It is questionable, however, whether graphite is suitable for the demanding modern applications (*e.g.*, electric/hybrid electric vehicles, portable tools and stationary storage of energy in conjunction with power grids and renewable sources) as it has a low theoretical capacity (*ca.* 372 mA h g^{-1}), approximately one-tenth of that of a Li anode.[6] For that reason material scientists are now searching for anode materials with improved lithium storage characteristics, and a number of prospective anode materials with much higher charge storage capacities have been identified.[7,8] Instead of relying on lithium intercalation into a layered host,[9,10] these promising materials operate *via* the alloying–dealloying or conversion reaction mechanisms, and capacities in excess of 1000 mA h g^{-1} may be feasible.[11,12]

Tin dioxide (SnO$_2$) and iron oxide (Fe$_2$O$_3$) are currently considered as some of the most practically attractive materials that react with lithium *via* the alloying–dealloying and conversion reaction mechanisms, respectively. SnO$_2$ converts into metallic tin in the first cycle of the battery's operation, and subsequent lithium storage happens *via* the reversible formation of tin–lithium alloys.[13,14] This mechanism provides a theoretical capacity of $\sim$780 mA h g^{-1} and makes tin dioxide attractive as an anode material. On the other hand, Fe$_2$O$_3$ has a theoretical capacity of 1007 mA h g^{-1} (based on the assumption of the reversible reduction of the oxide into metallic Fe) and is gaining considerable attention as the conversion reaction material of choice due to its abundant availability in nature, being environmentally benign and a relatively cheap price.[15,16]

A common issue with SnO$_2$ and Fe$_2$O$_3$ electrode materials delaying their commercial implementation is the significant volume change upon reaction with lithium, resulting in pulverisation and cracking of electrodes in the battery. Indeed, these materials experience a larger volume change of $\sim$300% for SnO$_2$ (ref. 1, 13 and 17) and $\sim$96% for Fe$_2$O$_3$,[18,19] respectively, and it is challenging to accommodate this level of volume alterations without damaging the structure of the electrode. Novel nanostructured electrode architectures are being researched as a method for tackling the problem. This concept is broadly based on downsizing the dimensions of individual particles to nanoparticles. Due to the small size, the nanoparticles can tolerate the strain associated with expansion much better. In addition, the nanoparticles should be connected in a proper way to form a "breathable" structure capable of

Institute for Frontier Materials, Deakin University, Waurn Ponds, VIC 3216, Australia. E-mail: m.rahman@deakin.edu.au; ian.chen@deakin.edu.au; Fax: +61352271103; Tel: +61352272642

† Electronic supplementary information (ESI) available: Electrochemical Impedance Spectroscopy (EIS). See DOI: 10.1039/c3nr00690e

expanding and contracting, and carbon coating and doping with foreign elements are used in some cases to improve the electronic conductivity of the electrode if required.[2,20–22]

An interesting strategy to combat the effects of a drastic volume change more effectively is to combine the two phases that react with lithium at different potentials *vs.* Li/Li$^+$ in one electrode. During the charge or discharge process in such an electrode, the volume expansion or contraction in the two phases is expected to happen sequentially, thus reducing the strain and improving the stability. Herein, we describe the preparation of nanostructured architecture of a Fe_2O_3–SnO_2 based electrode. The main active ingredient (Fe_2O_3 and SnO_2 nanoparticles) is present in the form of small clusters, providing "breathable" aggregates capable of effective sequential expansion and contraction. The aggregates of Fe_2O_3 and SnO_2 nanoparticles are dispersed on chains of conductive carbon in order to provide electronic conductivity in the electrode. We have selected Super P Li™, a specialised electrochemical carbon black from Timcal Ltd. as a conductive component of the electrode. One of the known advantages of the Super P Li™ carbon material is its one-dimensional chain-like structure of interconnected carbon particles. As we demonstrate, the low-energy ball milling with a dominating shear action serves as an excellent technique for spreading small clusters of oxide nanoparticles along the chains of Super P Li™ carbon black. The electrochemical performance of the electrode is superior to that of Fe_2O_3–SnO_2 electrode assembled *via* a conventional procedure. The structure and electrochemical performance of the composite electrode are discussed in this paper, and the performance is compared with those of Fe_2O_3–SnO_2 electrodes reported previously.

Experimental

Synthesis of Fe_2O_3–SnO_2 nanoparticles

The Fe_2O_3–SnO_2 powder was prepared by mixing $FeCl_2 \cdot 4H_2O$ (Sigma-Aldrich, 98%), $SnCl_2 \cdot 2H_2O$ (Sigma-Aldrich, 98%), $LiNO_3$ (Sigma-Aldrich, 99.9%), $LiOH \cdot H_2O$ (Sigma-Aldrich, 98%), and H_2O_2 (Sigma-Aldrich, 35%) in a molar ratio of 0.1 : 0.1 : 1.0 : 0.5 : 0.5, then grinding the mixture in a mortar with a pestle until it became homogenous. The mixture was then held at 120 °C for 24 h in a vacuum oven, followed by a further heat-treatment in air at 300 °C for 3 h in a muffle furnace. After cooling naturally in air, the Fe_2O_3–SnO_2 solid was separated from the eutectic mixture by washing with a large amount of de-ionized (DI) water and by centrifugation. The product was then dried under vacuum at 100 °C overnight to remove the residual water.

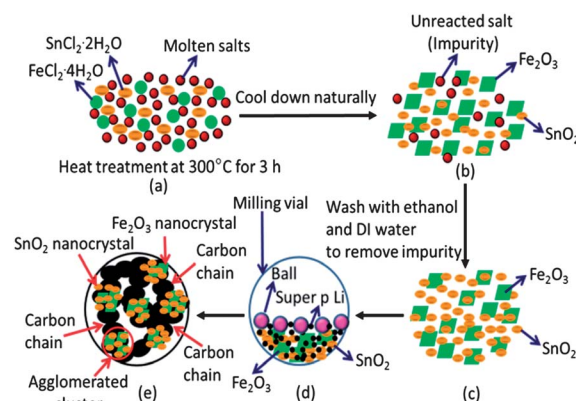### Preparation of Fe_2O_3–SnO_2–C nanocomposite

To prepare the Fe_2O_3–SnO_2–C nanocomposite, 600 mg of synthesised Fe_2O_3–SnO_2 powder and 300 mg of Super P Li™ in a weight ratio of 2 : 1 were loaded inside a stainless steel milling container together with four hardened steel balls (diameter of 25.4 mm). The powder was milled in a vertical rotating ball mill[23] at a rotation speed of 75 rpm for 25 h at room temperature

under an argon atmosphere of 100 kPa. This type of mill is usually used in conjunction with an external magnet; however, the magnet was intentionally removed in the preparation procedure to ensure a rolling action of the balls. In addition, the rotation speed (75 rpm) was intentionally selected low to ensure gentle milling. The overall materials preparation procedure is schematically described in Scheme 1.

Material characterization

X-ray diffraction (XRD) data were collected from powder samples on a PANalytical X'Pert Pro instrument using a CuKα radiation source ($\lambda = 1.54181$ Å) operated at 40 kV with 50 mA current. The scan rate and step angle were 2 s per step and 0.02°, and XRD data were collected over a range of 20–80°. The X'Pert data collector software in combination with the Joint Committee on Powder Diffraction Standards (JCPDS) powder diffraction files was used to identify the phases present. The Brunauer–Emmett–Teller (BET) surface area of the prepared materials was measured using a Tristar 3000 micrometrics gas adsorption analyser. The morphologies of the samples were examined by scanning electron microscopy (SEM, Carl Zeiss Supra 55vp Instrument). Transmission electron microscopy (TEM) investigations were performed using a JEOL JEM 2100F instrument operated at 200 kV. Energy-dispersive X-ray (EDX) maps and the corresponding bright-field image were acquired on the same microscope in scanning transmission electron microscopy (STEM) mode.

To test the electrochemical performance, the Fe_2O_3–SnO_2 powder sample was mixed with acetylene carbon black (AB) and a binder, carboxymethyl cellulose (CMC), in a weight ratio of 80 : 10 : 10 in a solvent (distilled water). It is important to note that acetylene carbon black (AB) was not added for the assembly of the Fe_2O_3–SnO_2–C electrode (weight ratio was 90% Fe_2O_3–SnO_2–C and 10% CMC). The slurry was spread onto Cu foil substrates and these coated electrodes were dried in a vacuum oven at 100 °C for 24 h. The electrode was then pressed using a disc with a diameter of 25 mm to enhance the contact between

Scheme 1 Schematic model of materials preparation procedure: (a) mixed raw materials heated at 300 °C for 3 h; (b) unreacted solid molten salts and Fe_2O_3–SnO_2 nanoparticles; (c) Fe_2O_3–SnO_2 nanoparticles; (d) milling; (e) final product of Fe_2O_3–SnO_2–C nanocomposite.

the Cu foil and active materials. Subsequently, the electrodes were cut to the size of 1×1 cm^2 and CR 2032 coin-type cells were assembled in an Ar-filled glove box (Innovative Technology, USA). Li foil was used as the counter/reference electrode and a microporous polyethylene film was used as a separator. The electrolyte was 1 M LiPF$_6$ in a mixture of ethylene carbonate (EC), diethylene carbonate (DEC), and dimethyl carbonate (DMC) with a volume ratio of 1 : 1 : 1. The cells were galvanostatically discharged–charged in the range of 0.01–3.0 V at different current densities using an Ivium-n-stat computer-controlled electrochemical analyser (Ivium Technologies, the Netherlands). Electrochemical impedance spectroscopy (EIS) was performed on the cells over the frequency range of 100 kHz to 0.01 Hz using the same instrument.

Results and discussion

The X-ray diffraction patterns of the Fe$_2$O$_3$–SnO$_2$ and Fe$_2$O$_3$–SnO$_2$–C samples are shown in Fig. 1. Both diffraction patterns indicate that the samples are composed of two phases. In both samples, diffraction peaks consistent with the rhombohedral phase of hematite Fe$_2$O$_3$ [space group $R\bar{3}c$ (no. 167), JCPDS no. 00-003-0800] and a tetragonal phase of cassiterite SnO$_2$ [JCPDS no. 00-002-1340, space group $P4_2/mnm$ (no. 136)] were observed. No peaks of any other phases or impurities were detected, demonstrating that materials with high purity could be obtained using the present synthesis strategy. The specific surface areas of the synthesised products were also measured by the N$_2$ adsorption/desorption method. The Fe$_2$O$_3$–SnO$_2$ sample showed the highest specific surface area (147 m^2 g^{-1}), while the Fe$_2$O$_3$–SnO$_2$–C sample had a specific surface area of 112 m^2 g^{-1}.

Fig. 2 shows SEM images of the Fe$_2$O$_3$–SnO$_2$ and Fe$_2$O$_3$–SnO$_2$–C samples. It is found that the Fe$_2$O$_3$–SnO$_2$ sample consists of agglomerated clusters of nanoparticles (Fig. 2(a)), which is consistent with the high surface area of the sample.[24] Furthermore, the Fe$_2$O$_3$–SnO$_2$ sample consists of two types of particles, fine and coarse. The tiny spherical particles (average diameter $\sim$ 2–10 nm) are SnO$_2$ and coarser cubic particles (average diameter $\sim$ 50–150 nm) are Fe$_2$O$_3$, as confirmed by the
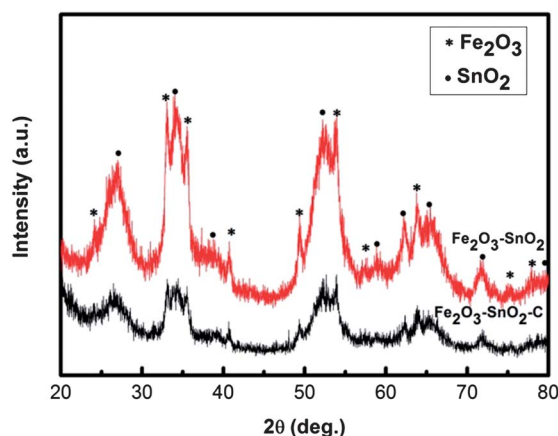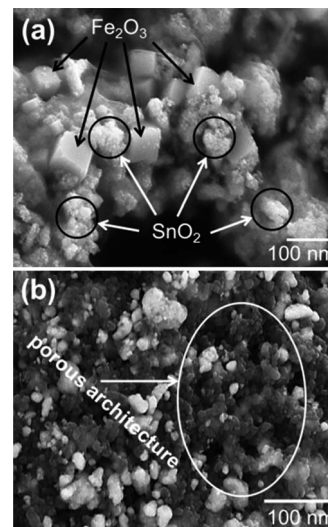
Fig. 2 SEM images of the Fe$_2$O$_3$–SnO$_2$ (a) and Fe$_2$O$_3$–SnO$_2$–C (b) powder samples.

subsequent TEM analysis. The SnO$_2$ and Fe$_2$O$_3$ nanoparticles are no longer clearly distinguishable in the Fe$_2$O$_3$–SnO$_2$–C sample (Fig. 2(b)), which has a relatively homogeneous mix of particles (compared to the Fe$_2$O$_3$–SnO$_2$ sample). Each of them has a smooth surface and a typical diameter of $\sim$2 to 50 nm with no obvious shape difference between SnO$_2$ and Fe$_2$O$_3$ particles. The reduction in the size of the Fe$_2$O$_3$ particles and changes in their shape are the result of the ball milling procedure used to prepare this sample. In addition to the SnO$_2$ and Fe$_2$O$_3$ particles, the Fe$_2$O$_3$–SnO$_2$–C sample contains Super P Li™ carbon black material. Understanding the structure and morphology of this sample from the SEM data alone is difficult, and additional TEM analysis was required for this purpose.

To obtain information concerning structural and morphological evolution of both samples, TEM measurements were carried out. Representative TEM images of the Fe$_2$O$_3$–SnO$_2$ sample are shown in Fig. 3(a) and (b). A bright-field image of a typical SnO$_2$ and Fe$_2$O$_3$ aggregate is presented in Fig. 3(a), and the inset shows the corresponding selected area electron diffraction (SAED) pattern. The pattern consists of two components, namely rings (originating from SnO$_2$) and a number of bright diffraction spots from scattered Fe$_2$O$_3$ particles. This type of pattern indicates that the aggregate consists of a large number of tiny particles of SnO$_2$ with random orientations and a small number of relatively large, strongly diffracting particles of Fe$_2$O$_3$. This is further demonstrated in Fig. 3(b), which is an image of a Fe$_2$O$_3$ crystal of 100–150 nm attached to an array of SnO$_2$ nanoparticles smaller than 10 nm. On the other hand, TEM observations of the Fe$_2$O$_3$–SnO$_2$–C sample are shown in Fig. 3(c)–(f). A bright-field image (Fig. 3(c)) indicates that the sample consists of long chains of Super P Li™ carbon black decorated with aggregates of nanoscale particles of oxides (darker contrast). The SAED pattern (Fig. 3(d)) consists of three components, a set of SnO$_2$ rings, discrete spots of Fe$_2$O$_3$, and a broad 002 ring of carbon black (overlapping with the 110 ring of SnO$_2$). Two marked areas from Fig. 3(c) containing
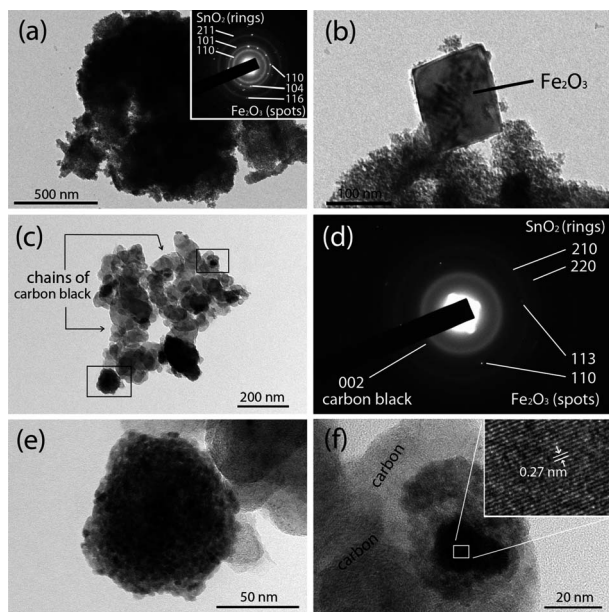

Fig. 1 X-ray diffraction patterns of Fe$_2$O$_3$–SnO$_2$–C and Fe$_2$O$_3$–SnO$_2$ samples.

Fig. 3 TEM images (a and b) of the Fe$_2$O$_3$–SnO$_2$ sample: (a) a bright-field image with its SAED pattern (inset) and (b) a Fe$_2$O$_3$ particle adjacent to the aggregated nanoparticles of SnO$_2$. TEM images (c–f) of the Fe$_2$O$_3$–SnO$_2$–C sample: (c and d) a bright-field image and its corresponding SAED pattern; (e) selected region (bottom mark) of (c) containing SnO$_2$ nanoparticles; (f) selected region (top mark) of (c) containing a Fe$_2$O$_3$ particle surrounded by SnO$_2$ nanocrystals with an HRTEM image (inset) revealing lattice fringes of the Fe$_2$O$_3$ crystal.

agglomerated oxide nanoparticles are magnified in Fig. 3(e) and (f). An aggregate of SnO$_2$ nanoparticles attached to carbon black chains is depicted in Fig. 3(e), and a more complex aggregate located on top of carbon black is presented in Fig. 3(f). The HRTEM analysis (inset) indicates that a larger nanoparticle in the middle of the aggregate is a crystal of Fe$_2$O$_3$.

Additional TEM characterisation was conducted in order to obtain elemental maps of the Fe$_2$O$_3$–SnO$_2$–C nanocomposite. A bright-field STEM image and the corresponding EDX elemental
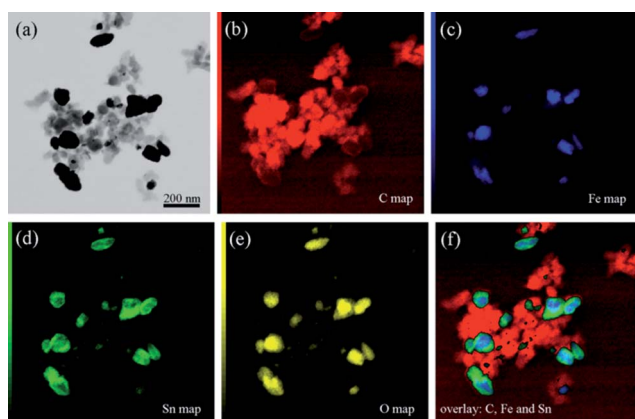
maps are shown in Fig. 4. The carbon map (Fig. 4(b)) depicts the location of interconnected Super P Li™ carbon black particles. The iron and tin maps are shown in Fig. 4(c) and (d), respectively. It can be concluded from comparing these two maps that tin oxide nanoparticles commonly surround iron oxide particles, creating composite structures similar to the one shown in Fig. 3(f). The oxygen map (Fig. 4(e)) matches the combination of iron and tin maps, which is consistent with the presence of oxides in the composite. Fig. 4(f) depicts an overlay of carbon, iron and tin maps, visualising directly distributions of carbon, iron oxide and tin oxide in the sample.

The electrochemical performance of the samples was evaluated using CR 2032 coin-type cells in which Li foil was used as the counter/reference electrode. The cells were galvanostatically discharged–charged in the range of 0.01–3.0 V at different current densities. Fig. 5(a) shows the comparison of the cycling performance of the Fe$_2$O$_3$–SnO$_2$ electrode at 158 mA g^{-1} current density with that of the Fe$_2$O$_3$–SnO$_2$–C electrode, and their corresponding discharge–charge voltage profiles are shown in Fig. 5(b) and (c). The measured 1st, 2nd, 15th, and 50th cycle discharge capacities were 1868, 1373, 1098, and 1006 mA h g^{-1} for the Fe$_2$O$_3$–SnO$_2$ electrode, and 1685, 1435, 1208, and 1110 mA h g^{-1} for the Fe$_2$O$_3$–SnO$_2$–C electrode, respectively. At the 50th cycle, the Fe$_2$O$_3$–SnO$_2$ electrode delivered a reversible capacity of 1006 mA h g^{-1}, which is 53% of the initial discharge capacity. In the case of the Fe$_2$O$_3$–SnO$_2$–C electrode, it was 1110 mA h g^{-1}, which is 66% of the initial discharge capacity. From this trend, it is clear that the capacity retention for the Fe$_2$O$_3$–SnO$_2$–C electrode is much better than that of the Fe$_2$O$_3$–SnO$_2$ electrode. The incorporation of Super P Li™ (a specialised electrochemical carbon black) in the Fe$_2$O$_3$–SnO$_2$–C nanocomposite provides a good conductive matrix, which not only maintains the integrity of the electrodes, but also decreases the cell polarization, thus enhancing the capacity retention for the Fe$_2$O$_3$–SnO$_2$–C electrode. The Coulombic efficiencies for the two electrodes are depicted in Fig. 5(d). The reversible capacities for

Fig. 4 Elemental maps of the Fe$_2$O$_3$–SnO$_2$–C nanocomposite: (a) a bright-field STEM image; (b–e) EDX maps of carbon, iron, tin and oxygen, respectively; (f) an overlay of carbon, iron and tin maps (colour scheme: carbon – red, iron – blue, tin – green). The level of detected signals is shown as a colour intensity bar on the left-hand side of each elemental map in (b–e).
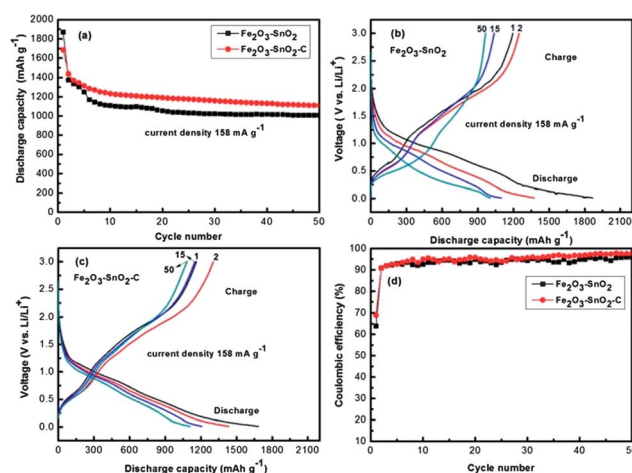
Fig. 5 Electrochemical performance of Fe$_2$O$_3$–SnO$_2$ and Fe$_2$O$_3$–SnO$_2$–C electrodes at 0.01–3.0 V: (a) cycling stability up to 50 cycles at 158 mA g^{-1}; (b and c) galvanostatic discharge–charge voltage profiles for the 1st, 2nd, 15th and 50th cycle at 158 mA g^{-1}; (d) corresponding Coulombic efficiencies.

both electrodes appear to be higher than the conventionally accepted theoretical capacities of the components, Fe_2O_3 (ref. 25–27) or SnO_2.[28–30] Such a high reversible capacity of the electrodes can be attributed to the synergistic electrochemical activity of the nanostructured Fe_2O_3 and SnO_2, reaching beyond the well-established mechanisms of charge storage in these two phases. According to the conventional understanding of the charge-storage mechanism in the SnO_2–Fe_2O_3 system, Li reacts with Fe_2O_3 *via* a reversible conversion reaction:[27,31]

$$Fe_2O_3 + 6Li^+ + 6e^- \leftrightarrow 2Fe + 3Li_2O \qquad (1)$$
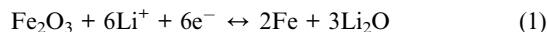
At the same time, SnO_2 is well known to have a two-step reaction with lithium, as expressed in the following eqn (2) and (3).[13,32]

$$SnO_2 + 4Li^+ + 4e^- \rightarrow Sn + 2Li_2O \qquad (2)$$

$$xLi^+ + xe^- + Sn \leftrightarrow Li_xSn \ (0 \leq x \leq 4.4) \qquad (3)$$
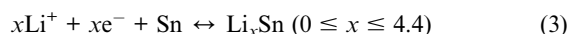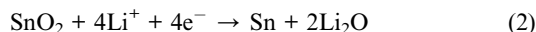
During the initial discharge, the SnO_2 nanoparticles convert into Sn and Li_2O by the irreversible initial reaction expressed in eqn (2). In the subsequent charge–discharge cycles, the capacity comes from the reversible formation of Li–Sn alloys. We hypothesize that the observed high capacities in the Fe_2O_3–SnO_2 and Fe_2O_3–SnO_2–C electrodes may be the result of a non-conventional mechanism such as partial reversibility of the initial conversion reaction (eqn (2)). Indeed, Guo *et al.*[33] have recently reported some experimental evidence of possible reversible conversion reaction in tin oxide electrodes. The Raman spectroscopy and TEM measurements of the SnO_2–carbon electrodes after the discharge and the subsequent charge in Li/SnO_2–C half-cell experiments have revealed the presence of SnO, implying that the reversible reaction:

$$Li_2O + Sn \leftrightarrow SnO + 2Li^+ + 2e^- \qquad (4)$$

may be operating, at least in the initial few cycles. Chen *et al.*[34] have proposed that the presence of a Fe-containing component in the composite Fe_2O_3–SnO_2 nanorattles leads to a significantly higher capacity of this electrode *via* making the initial conversion reaction of SnO_2 (eqn (2)) reversible. The capacity of the composite electrode was considerably higher than that of the electrode in pure (Fe_2O_3-free) SnO_2 nanospheres. The latter findings are in good agreement with our data. We have observed that the electrodes containing only SnO_2 nanoparticles and no Fe_2O_3 component have a capacity within the limit of the conventional theoretical capacity of 790 mA h g^{-1} for SnO_2. However, the possible lithium storage mechanism in the Fe_2O_3–SnO_2 system is described here. During discharge, Li is inserted first into the crystal structure of Fe_2O_3 at ~1.1 V as Li intercalation of Fe_2O_3 occurs at a higher voltage than that of SnO_2,[35–37] according to the conversion reaction described in eqn (1). This reaction yields metal nanoparticles of Fe, which can greatly increase the electrochemical reactivity. Therefore, nanoparticles of Fe can probably make extra Li_2O reversibly convert to Li^+ if there is any extra Li_2O present. During discharge, the SnO_2

nanoparticles can provide extra Li_2O by the irreversible initial reaction expressed in eqn (2). Hence, the presence of Fe nanoparticles may make extra Li_2O (provided by SnO_2) reversibly convert to Li^+, giving the electrodes higher reversible capacity.[38,39]

Additional examination of the electrochemical performance of the Fe_2O_3–SnO_2 and Fe_2O_3–SnO_2–C electrodes is shown in Fig. 6(a). The consecutive cycling behavior at different charge–discharge rates, measured after 10 cycles in ascending steps from 158 to 3950 mA g^{-1}, followed by a return to 158 mA g^{-1}, is presented. Galvanostatic discharge–charge voltage profiles for the 10th cycle at different charge–discharge rates (158, 790, 1580, and 3950 mA g^{-1}) are also depicted in Fig. 6(b) and (c). At the 10th cycle, the Fe_2O_3–SnO_2–C electrode showed a high reversible capacity of 1288 mA h g^{-1} at 158 mA g^{-1}, which changed to 990 mA h g^{-1} at 790 mA g^{-1} and 774 mA h g^{-1} at 1580 mA g^{-1}. In the case of the Fe_2O_3–SnO_2 electrode, it was 1136, 816, and 473 mA h g^{-1} at a current rate of 158, 790, and 1580 mA g^{-1}, respectively. It is also notable that the Fe_2O_3–SnO_2–C electrode could tolerate a high current rate and its reversible capacity was 502 mA h g^{-1} (still higher than the theoretical capacity of graphite, ~372 mA h g^{-1}) at the high current rate of 3950 mA g^{-1}. After 50 cycles with different charge–discharge rates, the reversible capacity of the Fe_2O_3–SnO_2–C electrode at 158 mA g^{-1} was still 1159 mA h g^{-1} (90% of the 10th cycle reversible capacity of 1288 mA h g^{-1} measured at 158 mA g^{-1}). This is an excellent cycling performance, even after cycling at high current rates, and is clearly much better than the performance of the Fe_2O_3–SnO_2 electrode. Fig. 6(d) shows the variation in the cell capacity as a function of the applied charge–discharge rate, expressed in mA g^{-1}. It is obvious that the Fe_2O_3–SnO_2–C electrode shows a very good rate capability as it has a markedly lower slope than the Fe_2O_3–SnO_2 electrode. The conducting carbon black component in the form of chains could increase the electron transfer and reduce the charge transfer resistance within the electrode,[27,40,41] leading to a better ability of the Fe_2O_3–SnO_2–C composite electrode to tolerate
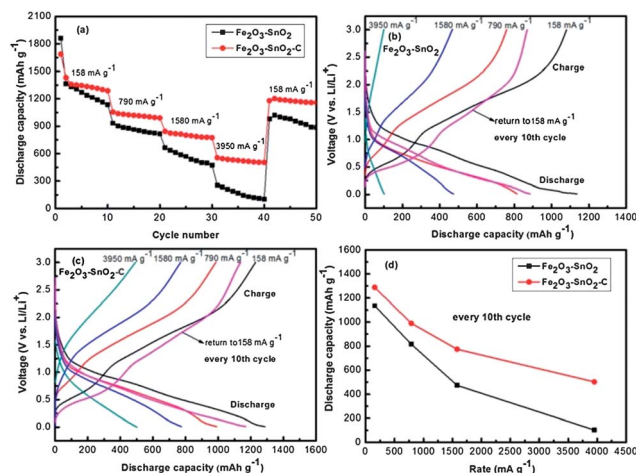

Fig. 6 Electrochemical performance of Fe_2O_3–SnO_2 and Fe_2O_3–SnO_2–C electrodes: (a) consecutive cycling behavior at different rates; (b and c) galvanostatic charge–discharge voltage profiles for every 10th cycle at each rate; (d) rate capability at different current rates.

high current rate. There is no significant difference in the discharge capacity between the two electrodes at the moderate current density of 158 mA g^{-1}. This could be reasonable because Li$^+$ insertion/extraction is sufficient at a relatively low charge–discharge rate. The difference between the lithium storage capacities of the electrodes increased with increasing charge–discharge rate and became significant at a very high current rate of 3950 mA g^{-1}. This result confirms that the chains of carbon black (Super P Li™) among the Fe$_2$O$_3$–SnO$_2$ particles can significantly improve the kinetics of the Fe$_2$O$_3$–SnO$_2$–C electrode, giving the Fe$_2$O$_3$–SnO$_2$–C electrode better rate capability.

To understand the electrode kinetics, electrochemical impedance spectra (EIS) for the Fe$_2$O$_3$–SnO$_2$ and Fe$_2$O$_3$–SnO$_2$–C electrodes were collected for the fresh cells (Fig. S1, ESI†). The Nyquist plots show one compressed semicircle in the high to medium frequency range. A comparison of the diameters of the semicircles indicates that the impedance of the Fe$_2$O$_3$–SnO$_2$ electrode is significantly larger than that of the Fe$_2$O$_3$–SnO$_2$–C electrode. The values of R_{ct} (charge transfer resistance) for the Fe$_2$O$_3$–SnO$_2$ and Fe$_2$O$_3$–SnO$_2$–C electrodes were calculated to be approximately 1457 Ω and 220 Ω, respectively. The much smaller R_{ct} of the Fe$_2$O$_3$–SnO$_2$–C electrode indicates that the carbon mixing can enable much easier charge transfer at the electrode–electrolyte interface, and consequently decrease the overall battery internal resistance. The electrode could accordingly possess higher reactivity and lower polarization.[24,41]

The excellent electrochemical performance of the Fe$_2$O$_3$–SnO$_2$–C nanocomposite electrode can be attributed to the elegant combination of SnO$_2$ and Fe$_2$O$_3$, two promising anode materials, into an integrated structure of small clusters dispersed on top of conductive chains of carbon black. The high surface area and clusters of SnO$_2$ and Fe$_2$O$_3$ nanoparticles enable better contact between active materials and the electrolyte, reducing the traverse time for both electrons and lithium ions.[27,40,41] The combination of two materials, SnO$_2$ and Fe$_2$O$_3$, provides breathable aggregates and makes sequential expansion and contraction of the electrode possible, mitigating the problems associated with volume change. The conducting chains of carbon black among the small clusters serve as a conductive scaffold that maintains a reliable electrical contact between SnO$_2$–Fe$_2$O$_3$ and the current collectors.[42,43] The presence of extra spaces between the carbon black particles and the clusters is also beneficial for diffusion of the electrolyte into the bulk of the electrode, providing fast transport channels for the Li ions, and more effectively accommodating the volume variation. All of these factors increase the structural stability of the electrode, leading to the superior electrochemical performance of the Fe$_2$O$_3$–SnO$_2$–C electrode.

The performance of the composite electrodes reported here is compared favourably to those of the SnO$_2$–Fe$_2$O$_3$-based electrodes reported in the literature. A few attempts of combining SnO$_2$ and Fe$_2$O$_3$ into a composite electrode have been reported.[34,38,42,44–46] Zeng et al.[44] have produced microelectrodes based on SnO$_2$–Fe$_2$O$_3$ composite nanotube arrays, capable of delivering higher gravimetric capacity (965 mA h g^{-1}) than that of previously reported Fe$_2$O$_3$ nanotube arrays[47] and better cyclic

stability than that of SnO$_2$ nanotube arrays.[48] Fe$_2$O$_3$–SnO$_2$ composite nanocombs and nano-heterostructures have been studied by Singaporean groups.[38,45] These composite structures demonstrated a modest electrochemical performance, with initial capacity gradually fading away over extended cycles. Another type of SnO$_2$–Fe$_2$O$_3$ heterostructure, representing sub-10 nm iron oxide rods on a micron-sized primary SnO$_2$ sheet, was evaluated by Wang et al.[46] and the capacity of 325 mA h g^{-1} was measured after 50 cycles. Chen et al.[34] have indicated that the performance of Fe$_2$O$_3$@SnO$_2$ nanorattles is superior to that of SnO$_2$ hollow nanospheres. Finally, Zhu et al.[42] have assessed the electrochemical properties of SnO$_2$ and Fe$_2$O$_3$ nanoparticles dispersed over reduced graphene oxide sheets, capable of delivering 958 mA h g^{-1} at the current density of 395 mA g^{-1}. The content of Fe$_2$O$_3$ nanoparticles in the last work was, however, rather low (weight ratio of 1 : 11 with respect to SnO$_2$), and the iron oxide nanoparticles were believed to contribute merely as spacers preventing the agglomeration of the SnO$_2$ nanoparticles. The performance of Fe$_2$O$_3$–SnO$_2$ and Fe$_2$O$_3$–SnO$_2$–C electrodes reported here is attractive with respect to the Fe$_2$O$_3$–SnO$_2$ electrodes reported previously.

Conclusions

A molten salt precipitation method in conjunction with ball milling was used to produce a Fe$_2$O$_3$–SnO$_2$–C nanocomposite anode with attractive electrochemical performance in Li-ion batteries. The transmission electron microscopy revealed that the nanocomposite was composed of relatively small clusters of SnO$_2$ and Fe$_2$O$_3$ nanoparticles dispersed along conductive chains of Super P Li™ carbon black (Timcal Ltd.). The performance of the nanocomposite was superior to that of a mixture of Fe$_2$O$_3$ and SnO$_2$ nanoparticles prepared by the molten salt precipitation method and assembled into an electrode by a conventional procedure. The nanocomposite electrode demonstrated the reversible capacity of 1159 mA h g^{-1} after 50 cycles operated at different charge–discharge rates, ascending steps from 158 to 3950 mA g^{-1}, followed by a return to 158 mA g^{-1}. The demonstrated electrochemical performance is attractive with respect to those of Fe$_2$O$_3$–SnO$_2$ and Fe$_2$O$_3$–SnO$_2$–C electrodes reported previously. The synthesis strategy can possibly be extended to produce other nanocomposites of functional oxides for advanced applications such as rechargeable lithium-ion batteries.

Acknowledgements

Notes and references

1 C.-M. Wang, W. Xu, J. Liu, J.-G. Zhang, L. V. Saraf, B. W. Arey, D. Choi, Z.-G. Yang, J. Xiao, S. Thevuthasan and D. R. Baer, *Nano Lett.*, 2011, **11**(5), 1874.

2 M. Gu, Y. Li, X. Li, S. Hu, X. Zhang, W. Xu, S. Thevuthasan, D. R. Baer, J.-G. Zhang, J. Liu and C. Wang, *ACS Nano*, 2012, **6**(9), 8439.

3 C. Jiang, E. Hosono and H. Zhou, *Nano Today*, 2006, **1**(4), 28.

4 Y. Wang and G. Cao, *Adv. Mater.*, 2008, **20**, 2251.

5 J. Jiang, Y. Li, J. Liu, X. Huang, C. Yuan and X. Wen (David) Lou, *Adv. Mater.*, 2012, **24**, 5166.

6 J. R. Dahn, T. Zheng, Y. Liu and J. Xue, *Science*, 1995, **270**, 590.

7 A. S. Aricò, P. Bruce, B. Scrosati, J.-M. Tarascon and W. van Schalkwijk, *Nat. Mater.*, 2005, **4**, 366.

8 L. Ji, Z. Lin, M. Alcoutlabi and X. Zhang, *Energy Environ. Sci.*, 2011, **4**, 2682.

9 M. Gu, I. Belharouak, J. Zheng, H. Wu, J. Xiao, A. Genc, K. Amine, S. Thevuthasan, D. R. Baer, J.-G. Zhang, N. D. Browning, J. Liu and C. Wang, *ACS Nano*, 2013, **7**(1), 760.

10 M. Gu, I. Belharouak, A. Genc, Z. Wang, D. Wang, K. Amine, F. Gao, G. Zhou, S. Thevuthasan, D. R. Baer, J.-G. Zhang, N. D. Browning, J. Liu and C. Wang, *Nano Lett.*, 2012, **12**(10), 5186.

11 J. Cabana, L. Monconduit, D. Larcher and M. R. Palacín, *Adv. Mater.*, 2010, **22**, E170.

12 P. G. Bruce, B. Scrosati and J.-M. Tarascon, *Angew. Chem., Int. Ed.*, 2008, **47**(16), 2930.

13 I. Courtney and J. R. Dahn, *J. Electrochem. Soc.*, 1997, **144**, 2045.

14 M. Winter and J. O. Besenhard, *Electrochim. Acta*, 1999, **45**, 31.

15 X. Zhu, Y. Zhu, S. Murali, M. D. Stoller and R. S. Ruoff, *ACS Nano*, 2011, **5**(4), 3333.

16 Y. Zhao, J. X. Li, Y. H. Ding and L. H. Guan, *Chem. Commun.*, 2011, **47**, 7416.

17 T. Brousse, R. Retoux, U. Herterich and D. M. Schleich, *J. Electrochem. Soc.*, 1998, **145**, 1.

18 N. Y. Nuli, P. Zhang, Z. P. Guo and H. K. Liu, *J. Electrochem. Soc.*, 2008, **155**, A196.

19 Y.-M. Lin, P. R. Abel, A. Heller and C. B. Mullins, *J. Phys. Chem. Lett.*, 2011, **2**, 2885.

20 N. Liu, H. Wu, M. T. McDowell, Y. Yao, C. Wang and Yi. Cui, *Nano Lett.*, 2012, **12**(6), 3315.

21 Y. Wang, H. Li, P. He, E. Hosono and H. Zhou, *Nanoscale*, 2010, **2**, 1294.

22 J. Liu and X.-W. Liu, *Adv. Mater.*, 2012, **24**, 4097.

23 T. Tao, A. M. Glushenkov, C. Zhang, H. Zhang, D. Zhou, Z. Guo, H. K. Liu, Q. Chen, H. Hu and Y. Chen, *J. Mater. Chem.*, 2011, **21**, 9350.

24 M. M. Rahman, J. Z. Wang, M. F. Hassan, S. Chou, Z. X. Chen and H. K. Liu, *Energy Environ. Sci.*, 2011, **4**, 952.

25 S. Y. Liu, J. Xie, Q. Pan, C. Y. Wu, G. S. Cao, T. J. Zhu and X. B. Zhao, *Int. J. Electrochem. Sci.*, 2012, **7**, 354.

26 D. Larcher, C. Masquelier, D. Bonnin, Y. Chabre, V. Masson, J. B. Leriche and J. M. Tarascon, *J. Electrochem. Soc.*, 2003, **150**, A133.

27 S. L. Chou, J. Z. Wang, D. Wexler, K. Konstantinov, C. Zhong, H. K. Liu and S. X. Dou, *J. Mater. Chem.*, 2010, **20**, 2092.

28 W. J. Lee, M. H. Park, Y. Wang, J. Y. Leed and J. Cho, *Chem. Commun.*, 2010, **46**, 622.

29 S. M. Paek, E. J. Yoo and I. Honma, *Nano Lett.*, 2009, **9**(1), 72.

30 J. Xie, S. Y. Liu, X. F. Chen, Y. X. Zheng, W. T. Song, G. S. Cao, T. J. Zhu and X. B. Zhao, *Int. J. Electrochem. Sci.*, 2011, **6**, 5539.

31 P. Poizot, S. Laruelle, S. Grugeon, L. Dupont and J. M. Tarascon, *Nature*, 2000, **407**, 496.

32 Y. Idota, T. Kubota, A. Matsufuji, Y. Maekawa and T. Miyasaka, *Science*, 1997, **276**, 1395.

33 X. W. Guo, X. P. Fang, Y. Sun, L. Y. Shen, Z. X. Wang and L. Q. Chen, *J. Power Sources*, 2013, **226**, 75.

34 J. S. Chen, C. M. Li, W. W. Zhou, Q. Y. Yan, L. A. Archer and X. W. Lou, *Nanoscale*, 2009, **1**, 280.

35 J. Zhu, Z. Lu, M. O. Oo, H. H. Hng, J. Ma, H. Zhang and Q. Yan, *J. Mater. Chem.*, 2011, **21**, 12770.

36 W. Zeng, F. Zheng, R. Li, Y. Zhan, Y. Li and J. Liu, *Nanoscale*, 2012, **4**, 2760.

37 B. Sun, J. Horvat, H. S. Kim, W. S. Kim, J. Ahn and G. Wang, *J. Phys. Chem. C*, 2010, **114**, 18753.

38 W. W. Zhou, C. W. Cheng, J. P. Liu, Y. Y. Tay, J. Jiang, X. Jia, J. Zhang, H. Gong, H. H. Hng, T. Yu and H. J. Fan, *Adv. Funct. Mater.*, 2011, **21**, 2439.

39 X. Y. Xue, Z. H. Chen, L. L. Xing, S. Yuan and Y. J. Chen, *Chem. Commun.*, 2011, **47**, 5205.

40 M. M. Rahman, J. Z. Wang, M. F. Hassan, D. Wexler and H. K. Liu, *Adv. Energy Mater.*, 2011, **1**, 212.

41 M. F. Hassan, M. M. Rahman, Z. Guo, Z. Chen and H. K. Liu, *J. Mater. Chem.*, 2010, **20**, 9707.

42 J. Zhu, Z. Lu, M. O. Oo, H. H. Hng, J. Ma, H. Zhang and Q. Yan, *J. Mater. Chem.*, 2011, **21**, 12770.

43 J. X. Zhu, T. Sun, J. S. Chen, W. H. Shi, X. J. Zhang, X. W. Lou, S. Mhaisalkar, H. H. Hng, F. Boey, J. Ma and Q. Y. Yan, *Chem. Mater.*, 2010, **22**, 5333.

44 W. Zeng, F. Zheng, R. Li, Y. Zhan, Y. Li and J. Liu, *Nanoscale*, 2012, **4**, 2760.

45 W. Zhou, Y. Y. Tay, X. Jia, D. Y. Y. Wai, J. Jiang, H. H. Hoon and T. Yu, *Nanoscale*, 2012, **4**, 4459.

46 Y. Wang, J. Xu, H. Wu, M. Xu, Z. Peng and G. Zheng, *J. Mater. Chem.*, 2012, **22**, 21923.

47 J. Liu, Y. Li, H. Fan, Z. Zhu, J. Jiang, R. Ding, Y. Hu and X. Huang, *Chem. Mater.*, 2010, **22**, 212.

48 J. Wang, N. Du, H. Zhang, J. Yu and D. Yang, *J. Phys. Chem. C*, 2011, **115**, 11302.